

Mapping the Milky Way bulge at high resolution: the 3D dust extinction, CO, and X factor maps

M. Schultheis¹, B.Q. Chen^{2,3}, B.W. Jiang³, O.A. Gonzalez⁴, R. Enokiy⁵, Y. Fukui⁵, K. Torii⁵, M. Rejkuba⁶, and D. Minniti^{7,8,9}

¹ Université de Nice Sophia-Antipolis, CNRS, Observatoire de Côte d'Azur, Laboratoire Lagrange, 06304 Nice Cedex 4, France
e-mail: mathias.schultheis@oca.eu

² Department of Astronomy, Peking University, Beijing, P. R. China, e-mail: bchen@pku.edu.cn

³ Department of Astronomy, Beijing Normal University, Beijing 100875, P.R.China, e-mail: bjiang@bnu.edu.cn

⁴ European Southern Observatory, Alonso de Cordova 3107, Vitacura, Santiago, Chile, e-mail: ogonzale@eso.org

⁵ Department of Physics, Nagoya University, Furo-cho, Chikusa-ku, Nagoya, Aichi, 464-8601, Japan

⁶ European Southern Observatory, Karl-Schwarzschild-Strasse 2, D-85748 Garching, Germany, e-mail: mrejkuba@eso.org

⁷ Departamento Astronomía y Astrofísica, Pontificia Universidad Católica de Chile, Av. Vicuña Mackenna 4860, Stgo., Chile, e-mail: dante@astro.puc.cl

⁸ Vatican Observatory, V00120 Vatican City State, Italy

⁹ Departamento de Ciencia Físicas, Universidad Andres Bello, Santiago, Chile

Preprint online version: March 1, 2022

ABSTRACT

Context. Three dimensional interstellar extinction maps provide a powerful tool for stellar population analysis. However, until now, these 3D maps were rather limited by sensitivity and spatial resolution.

Aims. We use data from the VISTA Variables in the Via Lactea survey together with the Besançon stellar population synthesis model of the Galaxy to determine interstellar extinction as a function of distance in the Galactic bulge covering $-10^\circ < l < 10^\circ$ and $-10^\circ < b < 5^\circ$.

Methods. We adopted a recently developed method to calculate the colour excess. First we constructed the H–Ks vs. Ks and J–Ks vs. Ks colour-magnitude diagrams based on the VVV catalogues that matched 2MASS. Then, based on the temperature-colour relation for M giants and the distance-colour relations, we derived the extinction as a function of distance. The observed colours were shifted to match the intrinsic colours in the Besançon model as a function of distance iteratively. This created an extinction map with three dimensions: two spatial and one distance dimension along each line of sight towards the bulge.

Results. We present a 3D extinction map that covers the whole VVV area with a resolution of $6' \times 6'$ for J–Ks and H–Ks using distance bins of 1 kpc. The high resolution and depth of the photometry allows us to derive extinction maps for a range of distances up to 10 kpc and up to 30 magnitudes of extinction in A_V (3.0 mag in A_{Ks}). Integrated maps show the same dust features and consistent values as other 2D maps. We discuss the spatial distribution of dust features in the line of sight, which suggests that there is much material in front of the Galactic bar, specifically between 5-7 kpc. We compare our dust extinction map with the high-resolution ^{12}CO maps (NANTEN2) towards the Galactic bulge, where we find a good correlation between ^{12}CO and A_V . We determine the X factor by combining the CO map and our dust extinction map. Our derived average value $X=2.5 \pm 0.47 \times 10^{20} \text{cm}^{-2} \text{K}^{-1} \text{km}^{-1} \text{s}$ is consistent with the canonical value of the Milky Way. The X-factor decreases with increasing extinction.

Key words. Galaxy: bulge, structure, stellar content – ISM: dust, extinction

1. Introduction

To study the 3D structure of the Galactic bulge one needs to know the 3D extinction correction. For example, the VISTA Variables in the Via Lactea (VVV) survey (Minniti et al. 2010) aims to obtain the 3D distribution of old RR Lyrae stars in the bulge. In the large-scale studies of the bulge giants, most of the authors do not know the distance to the individual objects and therefore assume that all the stars are at the same distance, they then use 2D maps to correct for extinction. We show here that these assumptions cause large errors.

The Galactic bulge is a main component of our Galaxy that contains a large amount of interstellar gas and dust. While there are a few low-extinction fields (such as Baade's window), most of the bulge is affected by high and clumpy interstellar absorption (see e.g. Schultheis et al. 1999; Gonzalez et al. 2012) that reaches extreme values of $A_V > 50^m$ (Schultheis et al. 2009)

close to the Galactic centre (GC). An exact knowledge of interstellar extinction is crucial to understand the different stellar populations in the Galactic bulge.

During the past decade several two dimensional interstellar dust extinction maps have been made for the Galactic bulge. Schultheis et al. (1999) and Dutra et al. (2003) presented for the first time high resolution ($2' \times 2'$) maps in the inner bulge ($-2^\circ < b < 2^\circ$) using DENIS and 2MASS data. Nidever et al. (2012) determined high-resolution A_{Ks} maps using GLIMPSE-I, GLIMPSE-II, and GLIMPSE-3d data based on the Rayleigh-Jeans colour-excess (RJCE) method. Based on the H–[4.5] colour, they mapped the interstellar absorption along the Galactic plane ($|b| < 2^\circ$) with a spatial resolution of $2'$.

The VVV survey covers about 315 sq.deg of the Galactic bulge ($-10^\circ < l < 10^\circ$ and $-10^\circ < b < 5^\circ$). Gonzalez et al. (2012) presented for the first time the complete extinction map

of the Bulge. They measured the mean (J–Ks) colour of the red clump giants in small subfields and compared them with a reference field (Baade’s window) to obtain reddening values $E(J-K_s)$ for the whole Bulge area with a resolution between $2'$ and $6'$. This map extends beyond the inner Milky Way Bulge to higher Galactic latitudes and is the most complete study extending up to $A_V \sim 35^m$, which are much higher extinction values than were determined in most previous studies. This high-resolution map allowed Gonzalez et al. (2012) to demonstrate A_{K_s} variation of up to 0.1 mag within a $30'$ field centred on Baade’s Window. In more reddened inner regions of the Bulge the extinction variation is much stronger over smaller spatial scales as well.

In addition to near-infrared, the optical surveys OGLE and MACHO (Sumi 2004; Kunder et al. 2008; Nataf et al. 2013) provided highly accurate extinction maps of Bulge fields located mainly in the intermediate and outer Bulge ($b > 2^\circ$). However, the disadvantage of optical extinction maps is the strong variation of the extinction coefficient for different lines of sight (see e.g. Udalski 2003; Nidever et al. 2012)

All these studies are 2D-maps that assume that all stars are located at a distance of ~ 8 kpc from the Sun with no distance information. Stellar population synthesis models of the Milky Way can be used to infer the three-dimensional distribution of interstellar extinction. Marshall et al. (2006) presented a 3D extinction model of the Galaxy by using the 2MASS data and the stellar population synthesis model of the Galaxy, the so-called Besançon model of the Galaxy (Robin et al. 2003). Assuming a distance–colour relation (e.g., J–Ks), they compared the observed colours for each line of sight with the synthetic ones and attributed the corresponding distances derived from the model.

However, the study of Marshall et al. (2006) is limited by the confusion limit of 2MASS in the Galactic bulge region and by the limiting sensitivity of 2MASS in highly extinguished regions ($A_V > 30^m$). Using a similar method, Chen et al. (2013) used the GLIMPSE data together with the VVV data, combining the improved Besançon model (Robin et al. 2012) to present colour-excess maps for six different combination of colours. Their maps agree excellently well with the red-clump extinction map of Gonzalez et al. (2012). The maps of Chen et al. are restricted to the inner Bulge ($-2^\circ < b < 2^\circ$), and both Marshall et al. (2006) and Chen et al. (2013) only have a spatial resolution of $15' \times 15'$, which is too coarse for most Bulge studies.

In this paper we use the bulge VVV data set that covers about ~ 315 sq. degrees to trace the 3D extinction at a high resolution of $6' \times 6'$. This resolution enables for the first time dereddening of stars in 3D studies of the entire Galactic bulge.

Furthermore, we use this information to evaluate the so-called X-factor, which relates the amount of CO and molecular hydrogen defined as

$$X = \frac{N_{H_2}}{W} \quad [\text{cm}^{-2}\text{K}^{-1}\text{km}^{-1}\text{s}], \quad (1)$$

where W is the CO brightness temperature and N_{H_2} is the column density of H_2 . Determining this factor empirically in different environments is important for studies of higher redshift sources where the X-factor has to be assumed, because it cannot be measured. Here we complement the VVV NIR dataset with the J=1-0 transition of the ^{12}CO map from the NANTEN2 telescope (Enokiya et al. 2014) to investigate the relation between the extinction due to dust and the CO emission in the innermost 200 pc region of the Milky Way.

Previous work has provided evidence of a constant X-factor in the Milky Way and in the Local Group with a value of

$10^{20}\text{cm}^{-2}\text{K}^{-1}\text{km}^{-1}\text{s}$ for the Galactic clouds (Solomon et al. 1987; Young & Scoville 1991; Dame et al. 2001). Glover & Mac Low (2011) derived a relationship between the X factor and the mean extinction by analysing the global properties of the X-factor in different molecular models. They found that the X-factor decreases with increasing mean extinction. Shetty et al. (2011) applied the radiative transfer calculation to the molecular clouds. They obtained a similar averaged X-factor for the Milky Way (about $2 \times 10^{20}\text{cm}^{-2}\text{K}^{-1}\text{km}^{-1}\text{s}$), but found a more complex relation between the X-factor and the extinction A_V for different models. We here determine the X-factor and correlate the CO gas distribution with our 3D interstellar-dust extinction map.

We first briefly introduce our data set and method in Sect. 2. In Sect. 3 we present the complete high-resolution 3D-extinction and compare our map with previous work. We discuss the comparison between our extinction maps and the CO map in Sect. 5. We conclude in Sect. 6.

2. Data, model, and method

We use the J, H, and Ks-band catalogues from the VVV survey. The observations cover about 315 sq.deg of the Galactic bulge with $-10 < l < 10^\circ$ and $-10 < b < 5^\circ$ (Saito et al. 2012a). Owing to saturation of the VVV data, the 2MASS catalogue was used for $K_s < 12\text{mag}$ sources, while the VVV catalogues cover $K_s > 12\text{mag}$. The VVV data processing, photometric catalogues construction, and a comparison between VVV and 2MASS is presented in detail in Gonzalez et al. (2011b). Gonzalez et al. (2012) used these catalogues to construct the complete high spatial resolution 2D extinction map of the Bulge using the red clump star technique, while Chen et al. (2013) based on the VVV and 2MASS low-resolution 3D extinction maps of the inner Bulge.

Our method of constructing a 3D extinction map is described in detail in Chen et al. (2013). We briefly summarize it here: We used the newly improved Besançon Galaxy model (Robin et al. 2012), which includes a two-component bar/bulge model and applied several important corrections: (i) a new temperature-colour relation for M giants using the isochrones from Girardi et al. (2010) and extending the grid in the T_{eff} vs. $\log g$ plane (see also Chen et al. 2013); (ii) in contrast to Marshall et al. (2006), we did not exclude M dwarfs from our analysis; (iii) we used bootstrapping to derive a more realistic uncertainty in our method; (iv) the completeness limit was calculated for each filter for each subfield and the observations and the model were cut accordingly.

The data from both the VVV survey and the Besançon model were divided into subfields of $6' \times 6'$ for which extinction and distances were calculated. First we added photometric errors and diffuse extinction to the intrinsic colours Co_{ins} of the model. We assumed a diffuse extinction of 0.7 mag/kpc in the V band and a constant photometric error of 0.05 mag (Saito et al. 2012a). The colours were then sorted for the observed and simulated data and normalised by the corresponding number of objects in each bin given by $n_{\text{bin}} = \text{floor}(\min([N_{\text{obs}}, N_{\text{bes}}])/100)$. N_{obs} and N_{bes} are the total number of observed stars (in each subfield) and the stars in the Besançon model. This ensured that we had at least 100 stars per bin. In each corresponding colour bin, the Co_{ins} of the stars from the model data and the Co_{obs} from the observational data were used to calculate the extinction using the following equations:

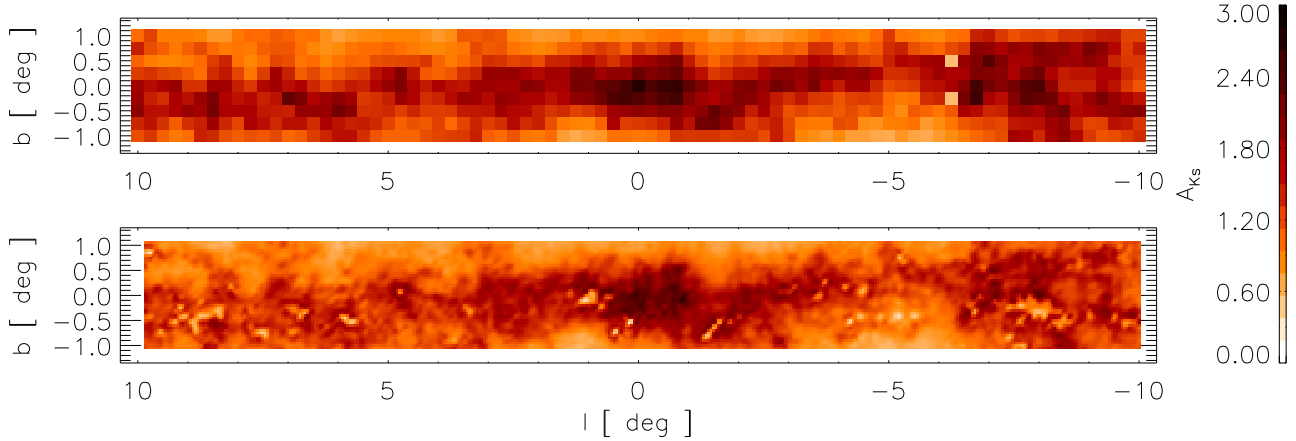
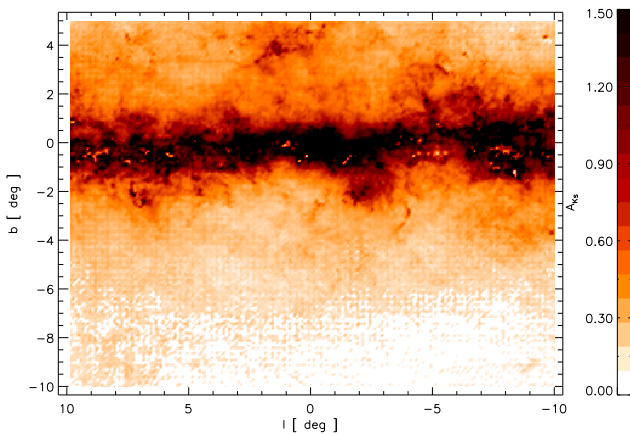
$$A_{K_s, J-K_s} = 0.528 \times \frac{((J-K_s)_{\text{obs}} - (J-K_s)_{\text{ins}})}{((H-K_s)_{\text{obs}} - (H-K_s)_{\text{ins}})}$$

$$A_{K_s, H-K_s} = 1.61 \times \frac{((H-K_s)_{\text{obs}} - (H-K_s)_{\text{ins}})}{((H-K_s)_{\text{obs}} - (H-K_s)_{\text{ins}})}$$

Table 1. Extinction as a function of Galactic longitude, latitude, and distance based on VVV data.

l	b	$E(J-K_s)_{1-10\text{kpc}}$	$E(H-K_s)_{1-10\text{kpc}}$	$\sigma E(J-K_s)_{1-10\text{kpc}}$	$\sigma E(H-K_s)_{1-10\text{kpc}}$
---	---	-----------------------------	-----------------------------	------------------------------------	------------------------------------

Notes. For each position we provide the $E(J-K_s)$, $E(H-K_s)$, and the corresponding sigma for each distance bin starting from 1 to 10 kpc.


Fig. 1. Visual comparison of the low-resolution extinction map (Chen et al. 2013) with our high-resolution map, integrated up to a distance of 8 kpc.

Fig. 2. 2D extinction A_{K_s} integrated at 8 kpc. The x-axis denotes the Galactic longitude, the y-axis the Galactic latitude.

We assumed the interstellar extinction law of Nishiyama et al. (2009). A first distance and extinction estimate were thus obtained and directly applied to the intrinsic magnitudes in the model, which provided a new simulated colour. We constructed histograms for each colour of the new simulated data and the observational data using the same bin size (0.05 mag). The χ^2 statistics (Press et al. 1992; Marshall et al. 2006) was then used to evaluate the similarity of the two histograms, given by

$$\chi^2 = \sum_j (\sqrt{N_{obs}/N_{sim}}n_{sim_j} - \sqrt{N_{sim}/N_{obs}}n_{obs_j})^2 / (n_{sim_j} + n_{obs_j}), \quad (2)$$

where N_{obs} and N_{sim} are the total number of observed and simulated stars in each subfield, while n_{obs_j} and n_{sim_j} show the number of stars for the j th colour bin of the observations and simulated

data. The first extinction estimate applied provided a new set of simulated data. In this new data set, some of the stars may be fainter and fall outside the completeness limit, while others may be brighter and now are inside the limit. The new simulated data were used iteratively to refine our results. In total, we performed 20 iterations for each subfield and each colour. The distance and extinction with the lowest χ^2 were our final result. The corresponding errors in the extinction and distances were calculated using the bootstrap method (see Chen et al. 2013 for further details).

The distance resolution depends on the chosen spatial resolution and the smallest number of stars, which is a function of the stellar density and the interstellar extinction. We set the smallest number of stars in the highest extinguished region to be 100 to ensure that a proper fit to the Besançon model can be still achieved. In less extinguished regions the number density will increase, giving a larger number of stars to fit the model. To resolve small-scale extinction features together with a decent distance resolution, our distance intervals were interpolated in bins of 500 pc with a spatial resolution of $6' \times 6'$.

3. High-resolution three-dimensional extinction maps

The complete high-resolution 3D extinction map for the region of the Bulge covered by the VVV survey will be available in electronic form at the CDS¹.

Table 1 provides an example of the format. Each row of Table 1 contains the information for one line of sight: Galactic coordinates along with the measured quantities for each distance bin $E(J-K_s)$, $E(H-K_s)$, and the respective uncertainties. These re-

¹ Table 1 is only available in electronic format from the CDS via anonymous ftp to cdsarc.u-strasbg.fr (130.79.128.5) or via <http://cdsweb.u-strasbg.fr/cgi-bin/qcat?J/A+A/>.

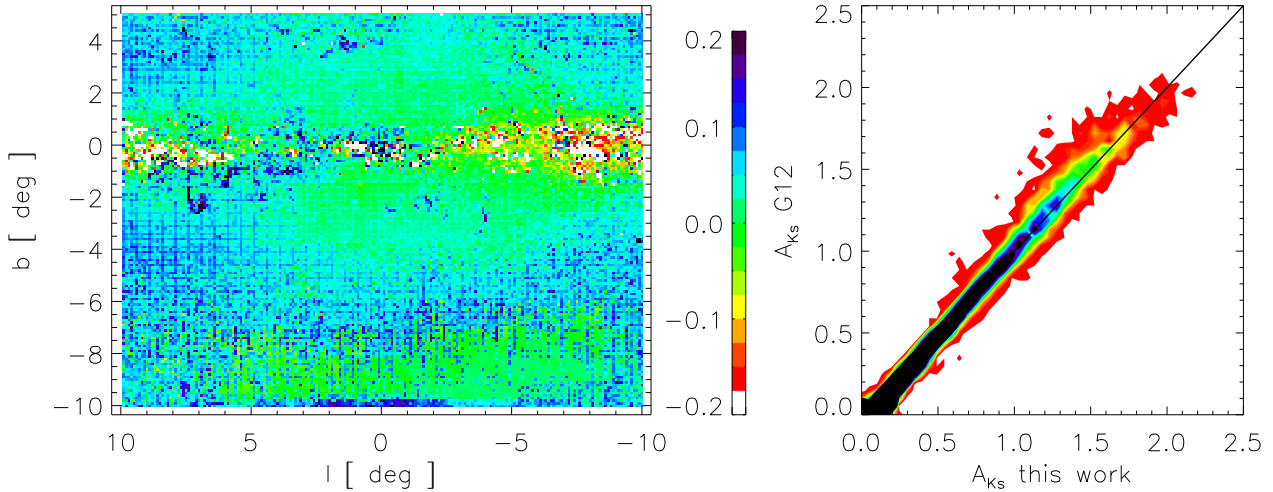


Fig. 3. Left panel: difference in the 2D extinction ($A_{KsG12} - A_{Ks}$) as a function of Galactic longitude and latitude compared with G12. Right panel: $A_{Ks\text{this work}}$ vs. A_{KsG12}

sults will also be available via the BEAM calculator² webpage (Gonzalez et al. 2012; Chen et al. 2013). Users of the BEAM calculator can choose to retrieve the extinction calculation with a specific reddening law and distance interval.

3.1. Integrated map at 8 kpc: the Galactic bulge extinction map

The three dimensional extinction maps allowed us to quantify the total amount of extinction that affects a source at a given distance, which results from the interstellar material distributed along the line of sight.

We first integrated our 3D extinction map up to a distance of 8 kpc to produce a 3D map in units of A_{Ks} . The projected map can be used to compare our results with the previously published 3D extinction maps from the literature.

As described in the previous section, we increased both the resolution and the coverage of the extinction map presented in Chen et al. (2013) and obtained from this the complete 3D extinction map for the VVV region of the Bulge. Figure 1 shows the comparison between the low-resolution (Chen et al. 2013) and high-resolution maps, both integrated up to a distance of 8 kpc. In general, we see very similar dust features. However, the fine filamentary structure of the dust extinction can only be resolved by the high-resolution map. The extinction, in the Galactic centre is so high that the VVV data does not contain enough stars for a small number of subfields (~ 10) when the high-resolution binning is used. These subfields were then filled-in the final high-resolution map by interpolating the lower resolution results (Chen et al. 2013). The complete extinction map of the Bulge, obtained by integrating our 3D map up to 8 kpc, is shown in Fig. 2.

Gonzalez et al. (2012) provided a complete high-resolution map ($2'-6'$) using the same data set, but they only used red clump stars as tracers of extinction. They selected the Bulge red clump stars for each line of sight from a CMD digram for each of the subfields and determined the interstellar extinction.

The red clump stars are a very homogeneous population where effects such as metallicity play only a minor role, and they are predominantly located in the bulge at approximately the

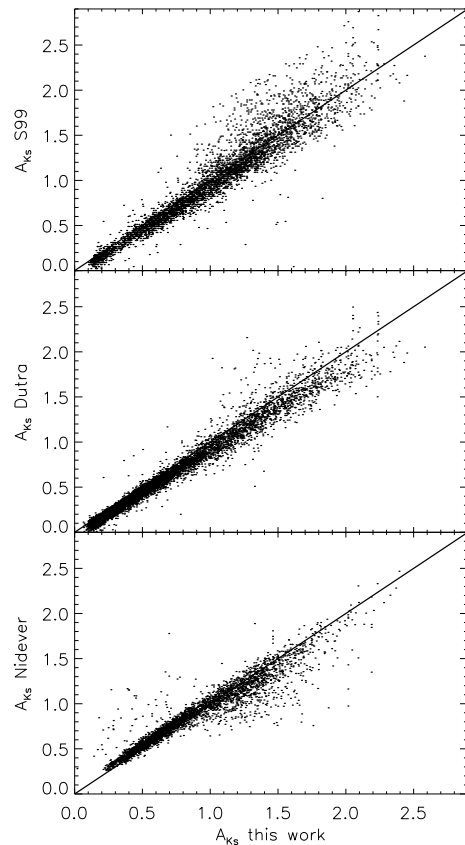


Fig. 4. Integrated 2D extinction at 8 kpc of our work compared with Schultheis et al. (1999, top panel), Dutra et al. (2003, middle panel) and Nidever et al. (2012, bottom panel). All maps have been transformed assuming the extinction law of Nishiyama et al. ($A_{Ks} = 0.528 \times E(J - Ks)$).

same distance, which makes them excellent tracers for the 2D extinction map. The difference between the mean (J–Ks) colour

² <http://mill.astro.puc.cl/BEAM/calculator.php>

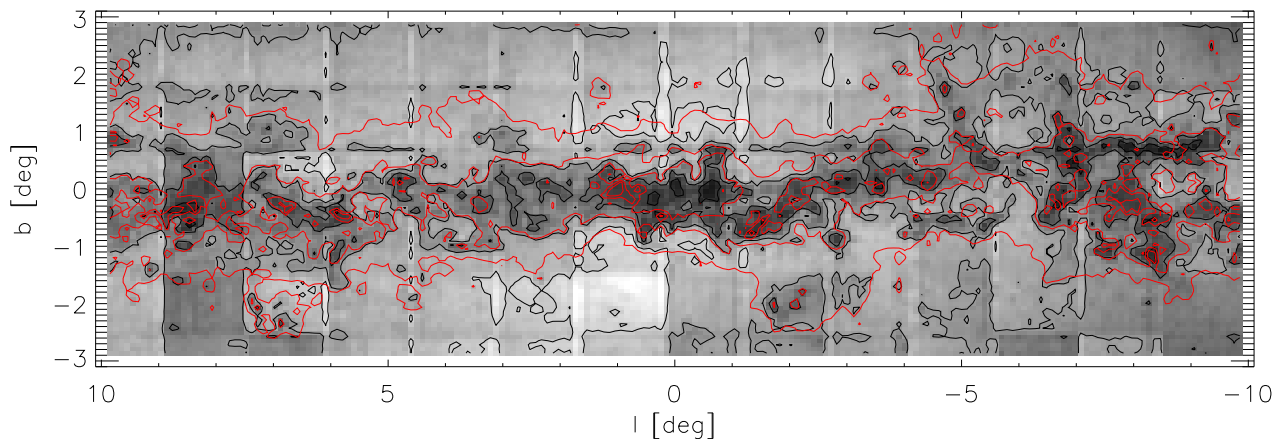


Fig. 5. Greyscale of the star count distribution together with the contour of the 2D extinction. The lower star density is denoted in black and higher star density in white. Note that stars were counted twice in the overlapping regions of the different tiles (seen as white vertical stripes).

of the selected RC stars for each subfield with respect to that of Baade’s Window, where the extinction is well known, was used to compute the average colour excess per subfield. We converted the $E(J - K_s)$ colour excesses of Gonzalez et al. (2012) into A_{K_s} using the Nishiyama extinction law ($A_{K_s} = 0.528 \times E(J - K_s)$) to compare it with our extinction map.

The left panel of Fig. 3 shows the difference ΔA_{K_s} between the map of Gonzalez et al. (G12) and our map as a function of Galactic longitude and latitude, the right panel shows A_{K_s} from our work vs. $A_{K_{sG12}}$. Although completely different methods were used to produce the maps, the two methods agree quite well, with a mean difference lower than 0.1 mag in A_{K_s} . This comparison shows that our maps are reliable. There is a larger scatter for highly extinguished regions ($A_{K_s} > 1.5$) located close to the Galactic plane. The number densities decreases quite significantly there (see Chen et al. 2013) and larger photometric uncertainties (due to the fainter K_s magnitudes) result in larger errors in A_{K_s} . The G12 map predicts higher extinction there, but as pointed out by Gonzalez et al. (2012), the RC stars in these very high extinction regions suffer from severe incompleteness.

Fig. 4 shows an additional comparison of the 2D extinction maps of Schultheis et al. (1999), Dutra et al. (2003), and Nidever et al. (2012). Schultheis et al. (1999) presented extinction maps for the inner Bulge with a very high spatial resolution ($2' \times 2'$). They used the DENIS near-infrared data set in combination with theoretical red giant branch (RGB)/asymptotic giant branch (AGB) isochrones from Bertelli et al. (1994). They showed that the observed sequence matched the isochrone with suitable reddening well for an appropriate sampling area. The highest extinction that could be reliably derived from the J and K_s data available from DENIS was about $A_V = 25^m$. Schultheis et al. (1999) found that in some areas, presumably those with the highest extinctions, no J-band counterparts for sources were detected in K_s . For these regions, only lower limits to the extinctions could be obtained. Dutra et al. (2003) obtained similar results using the same technique with 2MASS data. They presented the extinction map within 10° of the Galactic centre with a resolution of $4' \times 4'$.

Nidever et al. (2012) determined high-resolution A_{K_s} maps ($2'$) using GLIMPSE-I, GLIMPSE-II, and GLIMPSE-3d data

based on the Rayleigh-Jeans colour-excess (RJCE) method using the H-[4.5] colour, which is robust against spectral type. They obtained several extinction maps using RGB stars, RC stars, or their complete sample of stars. We used their “ALL” star catalogues. All maps were transformed using the Nishiyama et al. (2009) extinction law. All three maps show general agreement with our map. We note several differences: (i) Dutra et al. (2003) derived systematically lower extinction values; (ii) Schultheis et al. (1999) computed systematically larger extinction for highly extinguished regions, which might be mainly due to the completeness limit of DENIS; and (iii) the RJCE method in general shows the lowest dispersion and agrees even for the highest extinguished regions.

Figure 5 shows the number of stars in grey scale (the lower star density is denoted in black, the higher density in white) together with the contours of our extinction map. The number of stars and extinction are highly correlated, i.e.: the number density is smaller when the extinction is higher. We also also a structure at $||l| < 1$ and $|b| < 1$ with high extinction and small number densities, which might be related to the nuclear bar (see also e.g. Robin et al. 2012; Gonzalez et al. 2011a; Rodriguez-Fernandez & Combes 2008). However, the existence and the nature of this structure is still debated (see e.g. Gerhard & Martinez-Valpuesta 2012). The white vertical stripes in Fig. 5 are due to double counting of sources in the overlapping regions of the adjacent VVV tiles. We did not correct for these double sources here because it has no implication on the final results.

3.2. Integrated extinction map at different distances

2D maps for the Galactic bulge such as the one presented in Gonzalez et al. (2012) that are also based on the VVV data provide a measurement of integrated extinction at a fixed mean distance of ~ 8 kpc, which is the mean distance of the Bulge stars. These 2D maps very likely overestimate the extinction for sources located between us and the Galactic bulge.

As an example exercise, we consider two globular clusters in the direction of the Galactic bulge, NGC6626 and NGC6658, which have a distance modulus of 13.60 (5.2 kpc) and 14.30 (7.2 kpc) magnitudes, respectively (Chun et al. 2010). From the

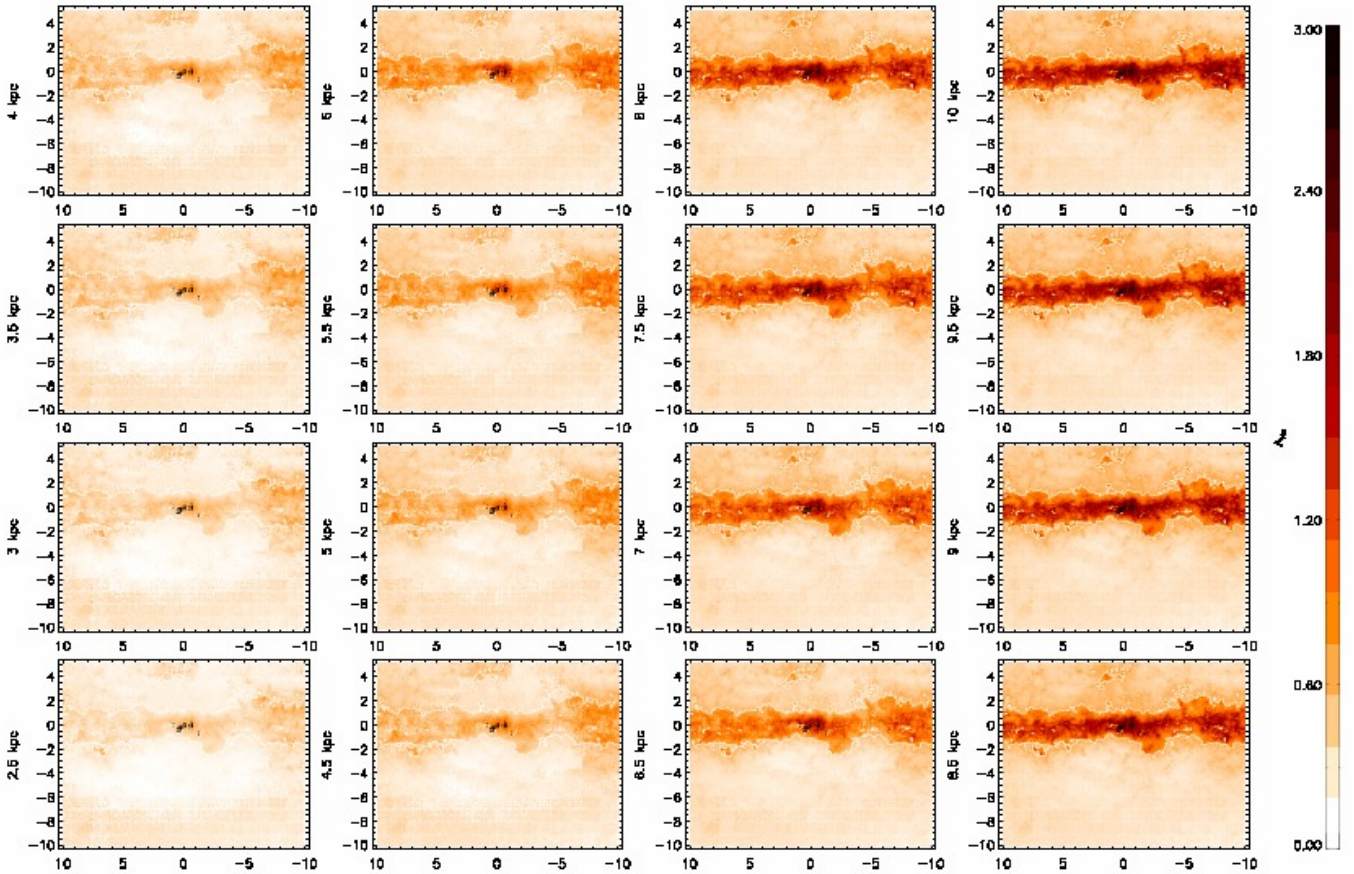


Fig. 6. Integrated 3D extinction A_{K_s} . The x-axis denotes the Galactic longitude, the y-axis the Galactic latitude. The units are $\delta A_{K_s} \text{ kpc}^{-1}$. The distances are given with respect to the sun. White contours mark the highest extinguished regions with $A_{K_s} \geq 0.8$. The tilt in the dust extinction with the negative longitude part located above the plane and the positive longitude below the plane is clearly seen. The indicated feature located at $l \sim 2^\circ$, $b \sim 4^\circ$ is the Pipe nebula.

3D extinction map we derive $A_K = 0.101$ for NGC6626 and $A_K = 1.294$ for NGC6658. If we were to take the extinction from the 2D map integrated to 8-kpc (which is typically assumed), the adopted reddening would be $A_K = 0.182$ and $A_K = 1.792$, resulting in an overestimation of approximately 0.7 and 4 magnitudes in A_V , respectively. Photometric studies of ages and metallicities from colour-magnitude diagrams would definitely be affected if the 2D map extinction value were used instead of the 3D extinction map for these sources along the line of sight.

Figure 6 shows examples of our integrated extinction map, projected at different distances from the Sun. The fine details of the dust structures at different distances are clearly visible in these high-resolution maps. The apparent tilt in the highest amount of dust extinction (indicated as white contours in Fig. 6) is also visible, with the negative longitude (far-side) part located above the plane and the positive longitude (near-side) part below the plane. This is probably due to the existence of the dust lanes (see Marshall et al. 2008). Additionally, because the sensitivity of VVV is higher than that of 2MASS, we are also able to trace the dust lanes at $|l| < 2^\circ$. Another feature seen in the maps is the Pipe nebula, which is located at about $l \sim 2^\circ$, $b \sim 4^\circ$, as part of the Ophiuchus dark cloud complex.

3.3. Differential extinction maps and the spatial distribution of dust features

Another application for our 3D map is that one can investigate the actual spatial distribution of the dust that is responsible for the stellar extinction of background sources. This can be investigated from our maps, as shown in Fig. 7, from the difference between the integrated extinctions of two subsequent distance bins $A_{K_s,(d+0.5)\text{kpc}} - A_{K_s,(d)\text{kpc}}$ (e.g. $A_{K_s,5\text{kpc}} - A_{K_s,4.5\text{kpc}}$).

Figure 8 shows another view of the extinction map, both an integrated and differential one, as seen from the North Galactic pole. In contrast what was reported in Marshall et al. (2006), we see a much smoother increase in extinction for the inner 5 kpc, while our extinction values increase beyond 5 kpc. We confirm the elongated structure, which is much more pronounced than in Marshall et al. (2006), and passes through the Galactic centre that is related to the dust bar.

Figure 9 shows the interstellar extinction A_{K_s} as a function of distance for several selected subfields at different Galactic latitudes located at $b=+1^\circ$ (left), $b=0^\circ$ (middle), and $b=-1^\circ$ (right). Different colours stand for different longitudes. As expected, the extinction increases with increasing distance. Depending on the chosen line of sight, the extinction changes in a different way. However, for most of the subfields, the extinction grows much faster between 5 and 7 kpc, which indicates that dust clouds are

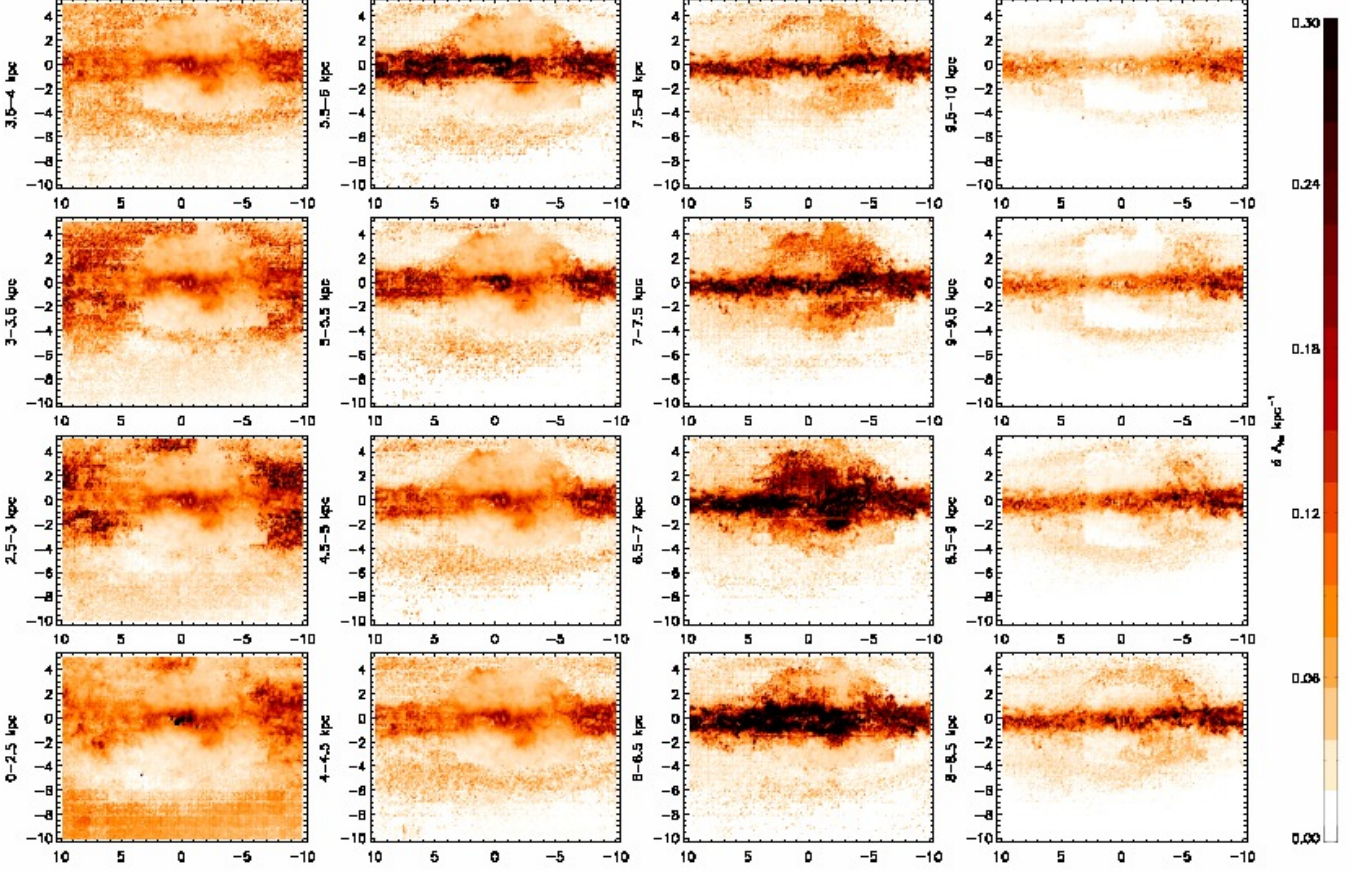


Fig. 7. Differential 3D extinction A_{K_s} . The x-axis denotes the Galactic longitude, the y-axis the Galactic latitude. The units are $\delta A_{K_s} \text{ kpc}^{-1}$. The distances are given with respect to the sun.

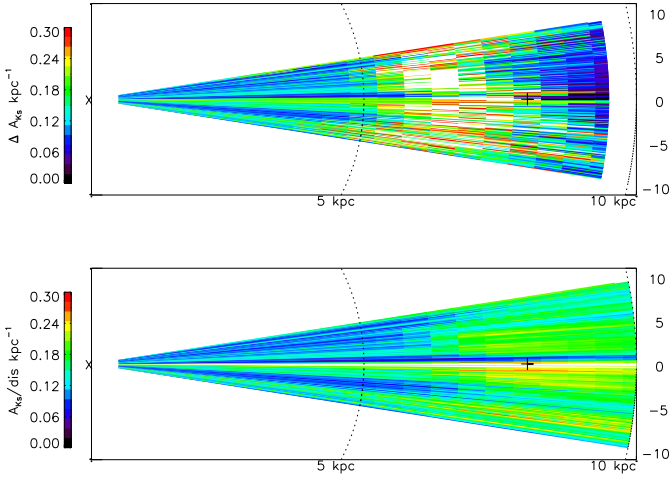


Fig. 8. Face-on view of the integrated dust extinction (lower panel) and the differential dust extinction (upper panel). The position of the sun is marked X and that of the Galactic centre +. The Galactic longitude is indicated on the y-axis.

clustered in this range of distance. The extinction grows only slowly after about 8 kpc, where in many cases the highest dust absorption is reached (see also Fig. 6). We also note that the dust distribution is non-axisymmetric along the major axis.

We clearly see that the peak in the extinction increases significantly at about 5–7 kpc and decreases after 8 kpc. This is at odds with the intuitive scenario of Galactic extinction, where this reaches a maximum at 8 kpc, that is, at the Galactic centre. An overdensity of material, strongly concentrated between 5–7 kpc, would then be required to explain the sudden increase of extinction seen at these distances in Fig. 7. Liu et al. (2012) investigated the extinction properties towards the anticentre direction, using spectra of disk red clump giants, and discovered extinction peaks at a Galactocentric distance of 9.5 and 12.5 kpc. They identified this feature as the dust lane of the Perseus spiral arm. This finding leads us to suggest a similar scenario, in this case in the direction of the Galactic centre, to explain the extinction peak between 5–7 kpc observed in our maps.

To test this possibility, we show in Fig. 10 the face-on view of the differential extinction map shown in Fig. 8 now overlaid on the illustration of the Galaxy produced by Robert Hurt of the Spitzer Science Centre that includes positions of HII+ MYSOs sources detected in the Galactic disk (adapted from Fig. 6 of Urquhart et al. 2014). The increase of extinction observed in our map shows no clear correlation with the expected location of the closer Galactic spiral arms. However, the distance at which the most dramatic increase of extinction occurs, as seen in Figs. 7 Fig. 9, is clearly located immediately in front of the Galactic bar and appears to follow the orientation angle of the bar. This would indicate that there is a high concentration of dust material, that is, a dust lane, in front of the Galactic bar.

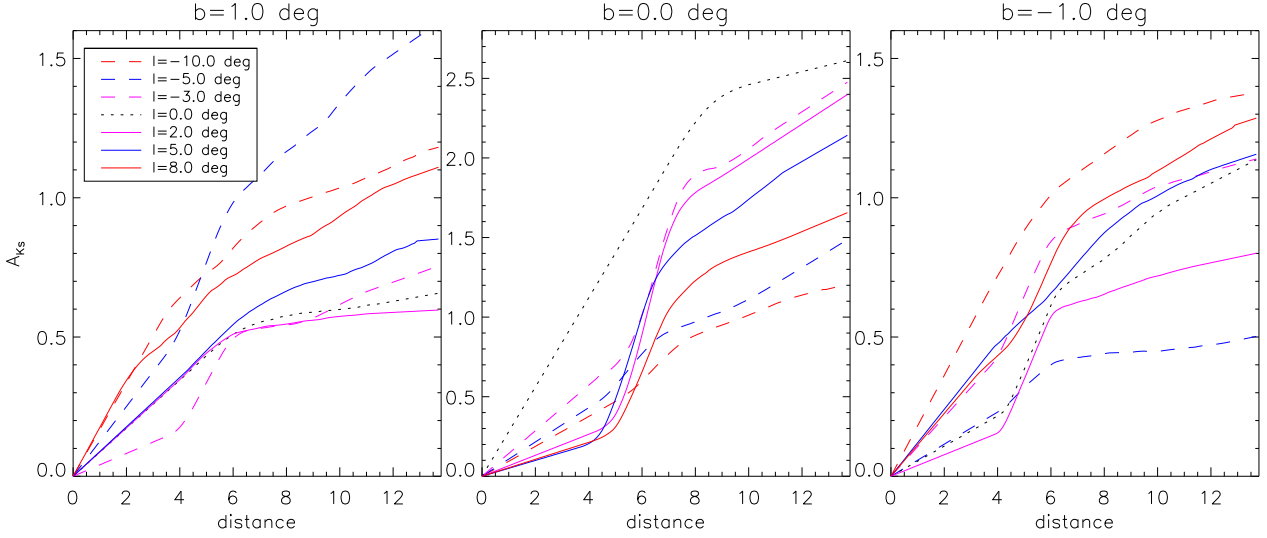


Fig. 9. Distance vs. A_{K_S} along different lines of sight. Different colours indicate different Galactic longitudes.

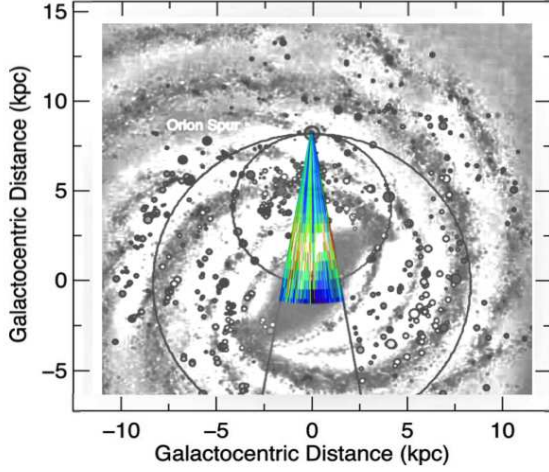


Fig. 10. Face-on view of the differential dust extinction shown overlaid on the illustration of the Milky Way produced by Robert Hurt and positions of HII+ MYSOs sources detected in the Galactic disk from Fig. 6 of Urquhart et al. (2014).

Alternatively, this peak of extinction at 5 kpc might be due to the so-called molecular ring (Stecker et al. 1975; Roman-Duval et al. 2010), a prominent feature in the CO emission (Dame et al. 2001) located around 4 kpc from the Galactic centre. The existence of this molecular ring is still debated. Dobbs & Burkert (2012) showed that most of the CO emission in the velocity-longitude space can be fitted by nearly symmetric two-armed spiral pattern, where one of the spiral arms corresponds to the molecular ring (Dobbs & Burkert 2012).

4. Application to stellar population synthesis models

Three dimensional extinction is an important ingredient for stellar population synthesis models. To compare the different stellar population synthesis models we applied our 3D extinction map

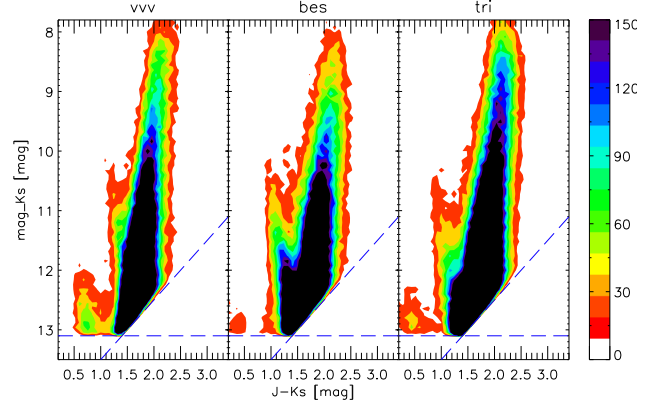


Fig. 11. J–Ks vs. Ks colour-magnitude diagram of the field at $l = 1.5^\circ$, $b = +1.5^\circ$. The left panel shows the VVV data, the middle panel the Besançon model, and the right panel the TRILEGAL model. For the two models (Besançon and Trilegal) the CMDs were broadened by adding our 3D extinction map.

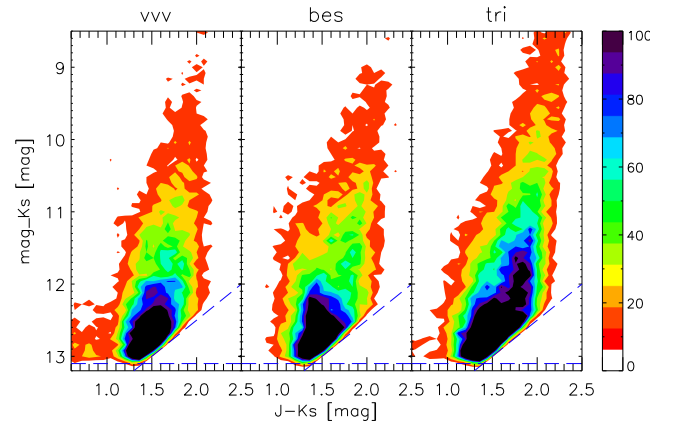


Fig. 12. Similar as Fig. 11, but for the field $l = 6^\circ$, $b = -2^\circ$.

also to the TRILEGAL model (Version 1.6). This allowed us to compare these two models in more detail. The TRILEGAL model was developed by Girardi et al. (2005) and is a population synthesis code for simulating the stellar photometry of any field in the Milky Way galaxy. The model has proven to reproduce number counts well, amongst others, in all three passbands of the 2MASS catalogue. The bulge component was introduced in TRILEGAL by Vanhollebeke et al. (2009), who also calibrated its stellar population and metallicity distribution using photometry from the 2MASS and OGLE-II surveys of red clump stars. Uttenthaler et al. (2012) and Saito et al. (2012b) first compared TRILEGAL and the Besançon model and found very similar colour-magnitude diagrams. Figure 11 shows a field in the inner Bulge located at $l = 1.5^\circ, b = +1.5^\circ$. To trace the differences we did not normalise the model data but compared the absolute numbers. We cut the catalogues by calculating the completeness limit of VVV, indicated by the dashed line (see Fig. 11). We clearly see here that our 3D extinction model matches the observed colour-magnitude diagram well. While models and the VVV data the two agree well in general, the Besançon model predicts a too large proportion of Galactic disk K giants, which has been noted by Chen et al. (2013). It also misses the brighter end of the Bulge sequence ($K < 8.5$), which is visible in TRILEGAL. Figure 12 shows another Bulge field located at $l = 6^\circ, b = -2^\circ$ with slightly lower extinction. Here the predicted colour distribution for both Besançon and TRILEGAL again agree well with the VVV observed one. The colours of the TRILEGAL model are slightly too red and the fraction of bright Bulge giants ($K_s < 10$) is too high. Again, the Besançon model shows a broadening of the CMD due to the K giants in the Galactic disk.

These two examples clearly show that the 3D extinction map allows a *systematic comparison* between stellar population synthesis models in general. Our derived 3D dust extinction depends on the stellar density, which is strongly model dependent. Using the same method but applied to the TRILEGAL model would reveal possible systematic differences in the 3D dust extinction map caused by the differences in the stellar population synthesis models.

5. Comparison with high-resolution CO data

Dust extinction at visible and near-infrared wavelengths is produced by large dust grains, which dominate the total dust mass of the galaxy, while the CO emission map traces the gas density and is very sensitive to the intrinsic properties of the gaseous medium, such as density, metallicity, and the background radiation field.

Enokiya et al. (2014) obtained observations of the J=1-0 transition of ^{12}CO with the NANTEN2 telescope using a high spatial resolution of $\sim 200''$. The observed CO intensity, $I(\text{CO})$, which is often expressed as an integrated brightness temperature (hereafter W), is considered to be a good tracer of the column density of molecular hydrogen N_{H_2} using a constant X-factor.

The observations were made in the OTF mode and the final r.m.s noise fluctuations are $0.5\text{--}1.0\text{ K}$ for a velocity resolution of 0.65 km s^{-1} . The data cover the inner region of the Bulge ($|l| < 10, |b| < 5$). We refer here to Enokiya et al. (2014) for a more detailed description of the data set.

We used the integrated CO map, which is in units of the brightness temperature (K). To compare our extinction map with the CO data, we smoothed the CO data to the same resolution as ours. Figure 13 shows the comparison of the dust extinction (lower panel) and the CO data (right panel). The gas and dust

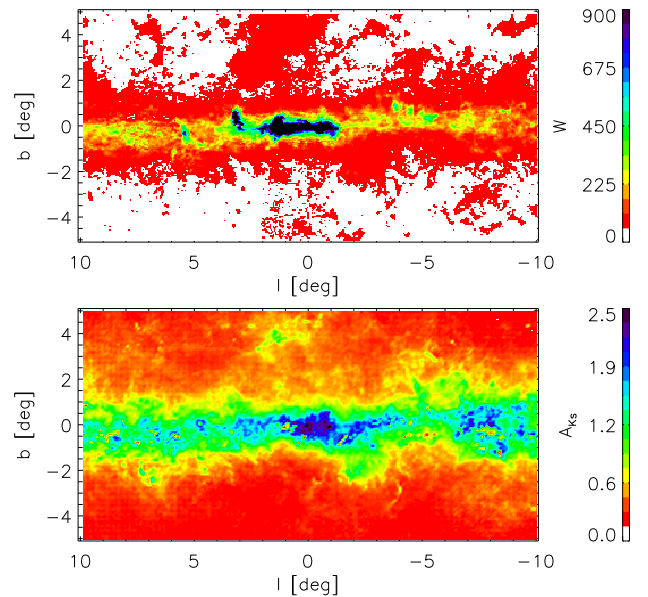


Fig. 13. Distribution of the CO (top) and the dust extinction map (bottom) for the inner Bulge.

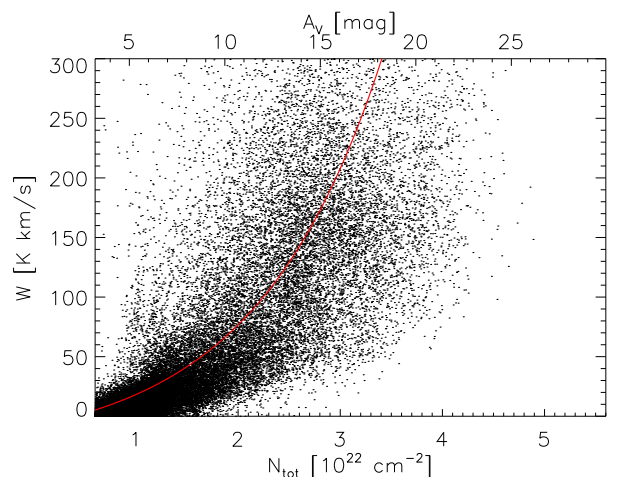


Fig. 14. CO intensity W as a function of the total column density N_H (bottom abscissa) or the extinction A_V (upper abscissa). The red line indicates the median values.

distribution concentrated on the Galactic plane ($|b| < 0.5$) are in general similar. The highest CO intensity and the highest the dust extinction occurs around the central molecular zone.

Extinction measurements provide estimates of the total amount of dust for different lines of sight. Assuming a certain reddening law (and an assumption for the dust-to-gas ratio), the total gaseous column follows directly from the amount of extinction A_V (Bohlin et al. 1978).

In most of the molecular clouds almost all the hydrogen is nearly molecular and can therefore be expressed as the total column density of the hydrogen nuclei N_H . We here applied the simple conversion between N_H and A_V (Shetty et al. 2011),

$$N_H = A_V * 1.87 \times 10^{21} / \left(\frac{Z}{Z_\odot}\right), \quad (3)$$

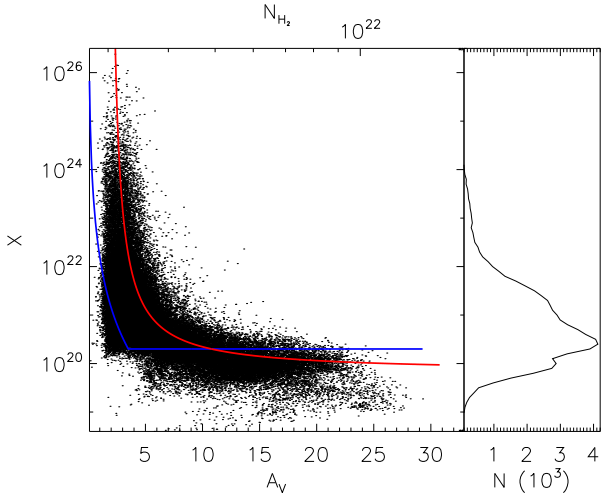


Fig. 15. X-factor plotted against N_{H_2} (left panel) and the histogram of the X-factor (right panel). Here we adopted $Z = 1.0Z_{\odot}$. The blue line shows the relation from Glover & Mac Low (2011).

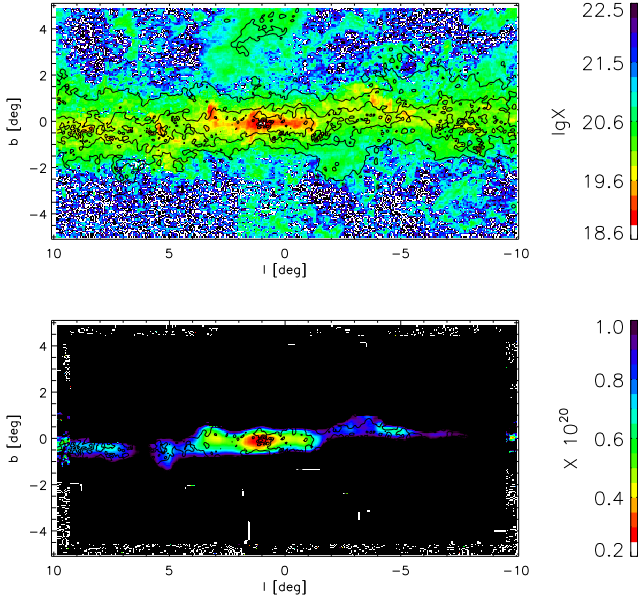


Fig. 16. Top panel: The variation of the X-factor as a function of Galactic longitude and latitude. The colour scale is logarithmic. Lower panel: smoothed map to a resolution of $40' \times 40'$ with a linear colour scale similar as in Regan (2000).

where Z is the metallicity of the gas.

To convert A_{K_S} into A_V we used the extinction law $A_V = A_{K_S}/0.089$ from Glass (1999). The metallicity in the Galactic bulge is still debated. Recent measurements indicate a solar iron abundance, but a high α -element value (see e.g. Zoccali et al. 2008; Hill et al. 2011; Gonzalez et al. 2011b; Bensby et al. 2013). We adopted $Z = 1.0 \times Z_{\odot}$. Fig. 14 shows the integrated CO intensity W as a function of the total column density N_H (bottom abscissa) or the extinction A_V . The red line indicates the median values. W increases with the increasing total column density. It shows a similar trend as predicted by detailed radiative transfer calculations of molecular clouds (see Fig. 1 from Shetty et al.

2011). We also note an increased dispersion in W with increasing extinction. A part of the high dispersion might also be due to the high metallicity dispersion in the Galactic bulge (> 0.5 dex). In addition, the gas pressure and temperature are higher, especially around the Galactic centre region, which leads to much higher CO intensities.

To use CO as a proxy for H_2 we used the X-factor, which is approximately constant for the Galactic disk molecular clouds. However, lower densities and metallicities increase the X-factor to higher values because of the lower CO excitation and CO/ H_2 ratios.

To obtain the X-factor, we derived the column density of H_2 . We used Tab. 2 from Glover & Mac Low (2011) to convert N_H into N_{H_2} . For the high densities in the Galactic bulge, we chose the model n1000, which means

$$N_{H_2} = N_H * 0.998/2. \quad (4)$$

Using the definition from Eq. 1, the X-factor can be calculated as follows:

$$X = N_{H_2}/W = (A_{K_S}/0.089) \times 0.935 \times 10^{21}/W. \quad (5)$$

We obtain an average value for $X = 2.5 \pm 0.47 \times 10^{20} \text{ cm}^{-2} \text{ K}^{-1} \text{ km}^{-1} \text{ s}$. This value is consistent with the canonical value of $X = 2 \times 10^{20} \text{ cm}^{-2} \text{ K}^{-1} \text{ km}^{-1} \text{ s}$ determined observationally for the Milky Way (Dame et al. 2001).

Figure 15 shows how the X-factor changes with extinction. The red line shows the following relation

$$X = 10^{20.0} - 10^{100 \cdot A_V + 150}. \quad (6)$$

Glover & Mac Low (2011) have demonstrated that the CO-to- H_2 conversion factor is determined primarily by the mean extinction of the cloud and that it is almost constant for $A_V > 3$. They reported that the X-factor declines from $X = 10^{24}$ to $X = 3 \times 10^{20} \text{ cm}^{-2} \text{ K}^{-1} \text{ km}^{-1} \text{ s}$ for A_V s in the range of $0.2 < A_V < 3$. We note a steady decrease of the X-factor with increasing extinction over the A_V -range $A_V < 10$ while a kind of flattening occurs at $A_V > 10$.

Our results show a very high dispersion of the X-factor for a given A_V that leads to a broad range of the X-factor of nearly a factor of 100 because of the extreme conditions in the Galactic bulge with its well-known high metallicity and velocity dispersion (e.g. Gonzalez et al. 2013; Howard et al. 2008; Babusiaux et al. 2010). The X-factor is known to depend on gas properties such as the temperature, density, metallicity, and its velocity field (Glover & Mac Low 2011; Papadopoulos et al. 2012). Narayanan & Hopkins (2013) used a combination of high-resolution galaxy evolution simulations to resolve giant molecular clouds (GMCs) and perform 3D molecular line radiative transfer calculations and found that the X-factor remains constant as a function of Galactocentric radius (see their Fig. 2). Figure 16 shows the variation of the X-factor as a function of the Galactic longitude and latitude. The very strong variation along individual lines of sight in the upper panel is expected because of large differences in the small-scale molecular cloud properties. The lower panel shows the map smoothed to a resolution of $40' \times 40'$, which corresponds to ~ 100 pc, a minimum spatial scale typically used in extragalactic studies where the X-factor is applied to an ensemble of molecular clouds (Regan 2000; Papadopoulos et al. 2012). Even in the smoothed map we clearly see the decrease of the X-factor in the Galactic centre region which indicates that the X-factor varies across the entire Bulge. The dispersion in X-factor measured from our maps is higher by a factor of 2 than that reported by Narayanan & Hopkins (2013).

It is interesting to compare our smoothed X-factor map (lower panel in Fig. 16) with the maps of the central regions of nearby spiral galaxies (Regan 2000). In these maps the X-factor is much lower (520 times) in the central regions than the value used locally in the Milky Way. The low X-factor values in the central regions of spiral galaxies agrees with our results, while the extremely low X-factors we derive for the central molecular zone in the Milky Way is typically not observed, which indicates extreme conditions in the central molecular zone.

6. Summary

Using an improved version of the Besançon model, we presented high-resolution 3D extinction maps ($6' \times 6'$) for the entire VVV bulge region. All extinction maps are available online at the CDS (Table 1) or through the BEAM calculator webpage (<http://mill.astro.puc.cl/BEAM/calculator.php>). Owing to the high sensitivity of the VVV data, we were able to trace high extinction until 10 kpc. Our maps integrated along the line of sight up to 8 kpc agree excellently well with the 2D maps from Schultheis et al. (1999), Dutra et al. (2003), Nidever et al. (2012), and Gonzalez et al. (2012). These maps show the same dust features and consistent A_{K_s} values. These 3D maps are a powerful tool in combination with stellar population synthesis models such as TRILEGAL.

Using high-resolution ^{12}CO maps from NANTEN2 (Enokiya et al. 2014) in the central molecular zone, we detected similar features in the gas and the dust. Assuming that all hydrogen is molecular and the mean metallicity is around solar, we were able to determine the X-factor with a mean value of $X = 2.5 \pm 0.47 \times 10^{20} \text{cm}^{-2} \text{K}^{-1} \text{km}^{-1} \text{s}$. Our mean value is consistent with the canonical value of molecular clouds in the Milky Way (Dame et al. 2001) and a high dispersion around the mean.

Acknowledgements. We thank the anonymous referee for his/her helpful comments. We thank Padelis Papadopoulos for the very informative discussion about the molecular gas and X-factor measurements in galaxies. We gratefully acknowledge use of data from the ESO Public Survey program ID 179.B-2002 taken with the VISTA telescope, data products from the Cambridge Astronomical Survey Unit, the BASAL CATA Center for Astrophysics and Associated Technologies PFB-06, the MILENIO Milky Way Millennium Nucleus from the Ministry of Economy ICM grant P07-021-F, and the FONDECYT the Proyecto FONDECYT Regular No. 1130196. B.Q.C was supported by a scholarship of the China Scholarship Council (CSC).

References

Babusiaux, C., Gómez, A., Hill, V., et al. 2010, *A&A*, 519, A77
 Bensby, T., Yee, J. C., Feltzing, S., et al. 2013, *A&A*, 549, A147
 Bertelli, G., Bressan, A., Chiosi, C., Fagotto, F., & Nasi, E. 1994, *A&AS*, 106, 275
 Bohlin, R. C., Savage, B. D., & Drake, J. F. 1978, *ApJ*, 224, 132
 Chen, B. Q., Schultheis, M., Jiang, B. W., et al. 2013, *A&A*, 550, A42
 Chun, S.-H., Kim, J.-W., Shin, I.-G., et al. 2010, *A&A*, 518, A15
 Dame, T. M., Hartmann, D., & Thaddeus, P. 2001, *ApJ*, 547, 792
 Dobbs, C. L. & Burkert, A. 2012, *MNRAS*, 421, 2940
 Dutra, C. M., Santiago, B. X., Bica, E. L. D., & Barbuy, B. 2003, *MNRAS*, 338, 253
 Enokiya, R., Torii, K., Schultheis, M., et al. 2014, *ApJ*, 780, 72
 Gerhard, O. & Martínez-Valpuesta, I. 2012, *ApJ*, 744, L8
 Girardi, L., Groenewegen, M. A. T., Hatziminaoglou, E., & da Costa, L. 2005, *A&A*, 436, 895
 Girardi, L., Williams, B. F., Gilbert, K. M., et al. 2010, *ApJ*, 724, 1030
 Glass, I. S. 1999, *Handbook of Infrared Astronomy*, ed. R. Ellis, J. Huchra, S. Kahn, G. Rieke, & P. B. Stetson
 Glover, S. C. O. & Mac Low, M.-M. 2011, *MNRAS*, 412, 337
 Gonzalez, O. A., Rejkuba, M., Minniti, D., et al. 2011a, *A&A*, 534, L14
 Gonzalez, O. A., Rejkuba, M., Zoccali, M., et al. 2013, *A&A*, 552, A110

Gonzalez, O. A., Rejkuba, M., Zoccali, M., Valenti, E., & Minniti, D. 2011b, *A&A*, 534, A3
 Gonzalez, O. A., Rejkuba, M., Zoccali, M., et al. 2012, *A&A*, 543, A13
 Hill, V., Lecureur, A., Gómez, A., et al. 2011, *A&A*, 534, A80
 Howard, C. D., Rich, R. M., Reitzel, D. B., et al. 2008, *ApJ*, 688, 1060
 Kunder, A., Popowski, P., Cook, K. H., & Chaboyer, B. 2008, *AJ*, 135, 631
 Liu, C., Xue, X., Fang, M., et al. 2012, *ApJ*, 753, L24
 Marshall, D. J., Fux, R., Robin, A. C., & Reylé, C. 2008, *A&A*, 477, L21
 Marshall, D. J., Robin, A. C., Reylé, C., Schultheis, M., & Picaud, S. 2006, *A&A*, 453, 635
 Minniti, D., Lucas, P. W., Emerson, J. P., et al. 2010, *New A*, 15, 433
 Narayanan, D. & Hopkins, P. F. 2013, *MNRAS*, 433, 1223
 Nataf, D. M., Gould, A., Fouqué, P., et al. 2013, *ApJ*, 769, 88
 Nidever, D. L., Zasowski, G., & Majewski, S. R. 2012, *ApJS*, 201, 35
 Nishiyama, S., Tamura, M., Hatano, H., et al. 2009, *ApJ*, 696, 1407
 Papadopoulos, P. P., van der Werf, P., Xilouris, E., Isaak, K. G., & Gao, Y. 2012, *ApJ*, 751, 10
 Press, W. H., Teukolsky, S. A., Vetterling, W. T., & Flannery, B. P. 1992, *Numerical recipes in FORTRAN. The art of scientific computing*
 Regan, M. W. 2000, *ApJ*, 541, 142
 Robin, A. C., Marshall, D. J., Schultheis, M., & Reylé, C. 2012, *A&A*, 538, A106
 Robin, A. C., Reylé, C., Derrière, S., & Picaud, S. 2003, *A&A*, 409, 523
 Rodríguez-Fernández, N. J. & Combes, F. 2008, *A&A*, 489, 115
 Roman-Duval, J., Jackson, J. M., Heyer, M., Rathborne, J., & Simon, R. 2010, *ApJ*, 723, 492
 Saito, R. K., Hempel, M., Minniti, D., et al. 2012a, *A&A*, 537, A107
 Saito, R. K., Minniti, D., Dias, B., et al. 2012b, *A&A*, 544, A147
 Schultheis, M., Ganesh, S., Simon, G., et al. 1999, *A&A*, 349, L69
 Schultheis, M., Sellgren, K., Ramírez, S., et al. 2009, *A&A*, 495, 157
 Shetty, R., Glover, S. C., Dullemond, C. P., & Klessen, R. S. 2011, *MNRAS*, 412, 1686
 Solomon, P. M., Rivolo, A. R., Barrett, J., & Yahil, A. 1987, *ApJ*, 319, 730
 Stecker, F. W., Solomon, P. M., Scoville, N. Z., & Ryter, C. E. 1975, *ApJ*, 201, 90
 Sumi, T. 2004, *MNRAS*, 349, 193
 Takeuchi, T., Yamamoto, H., Torii, K., et al. 2010, *PASJ*, 62, 557
 Udalski, A. 2003, *ApJ*, 590, 284
 Urquhart, J. S., Figura, C. C., Moore, T. J. T., et al. 2014, *MNRAS*, 437, 1791
 Uttenthaler, S., Schultheis, M., Nataf, D. M., et al. 2012, *A&A*, 546, A57
 Vanhollebeke, E., Groenewegen, M. A. T., & Girardi, L. 2009, *A&A*, 498, 95
 Young, J. S. & Scoville, N. Z. 1991, *ARA&A*, 29, 581
 Zoccali, M., Hill, V., Lecureur, A., et al. 2008, *A&A*, 486, 177